Chandra Multiwavelength Project. II. First Results of X#Ray Source Properties

Citation
Kim, D.#W., B. J. Wilkes, P. J. Green, R. A. Cameron, J. J. Drake, N. R. Evans, P. Freeman, et al. 2004. "Chandra Multiwavelength Project. II. First Results of X#Ray Source Properties." The Astrophysical Journal 600 (1) (January): 59–69. doi:10.1086/379820.

Published Version
doi:10.1086/379820

Permanent link
http://nrs.harvard.edu/urn-3:HUL.InstRepos:30238007

The Astrophysical Journal, 600:59–69, 2004 January 1 Ⓔ

CHANDRA MULTIWAVELENGTH PROJECT. II. FIRST RESULTS OF X-RAY SOURCE PROPERTIES

D.-W. Kim, B. J. Wilkes, P. J. Green, R. A. Cameron, J. J. Drake, N. R. Evans, P. Freeman, T. J. Gaetz, H. Ghosh, F. R. Harnden, Jr., M. Karovska, V. Kashyap, P. W. Maksym, P. W. Ratzlaff, E. M. Schlegel, J. D. Silverman, H. D. Tananbaum, and A. A. Vikhlinin
Smithsonian Astrophysical Observatory, 60 Garden Street, Cambridge, MA 02138
Received 2003 June 20; accepted 2003 August 24

ABSTRACT

The *Chandra* Multiwavelength Project (ChaMP) is a wide-area ($\sim$14 deg^2) survey of serendipitous *Chandra* X-ray sources, aiming to establish fair statistical samples covering a wide range of characteristics (such as absorbed active galactic nuclei [AGNs] and high-z clusters of galaxies) at flux levels ($f_{\rm X} \sim 10^{-15}$ to 10^{-14} ergs s^{-1} cm^{-2}) intermediate between the *Chandra* Deep Field surveys and previous missions. We present the first results of X-ray source properties obtained from the initial sample of 62 observations. The data have been uniformly reduced and analyzed with techniques specifically developed for the ChaMP and then validated by visual examination. Utilizing only near–on-axis X-ray–bright sources (to avoid problems caused by incompleteness and the Eddington bias), we derive the $\log N - \log S$ relation in soft (0.5–2 keV) and hard (2–8 keV) energy bands. The ChaMP data are consistent with previous results of *ROSAT*, *ASCA*, and *Chandra* Deep Field surveys. In particular, our data nicely fill in the flux gap in the hard band between the Chandra Deep Field data and the previous *ASCA* data. We check whether there is any systematic difference in the source density between cluster and noncluster fields and also search for field-to-field variation, both of which have been previously reported. We found no significant field-to-field cosmic variation in either test within the statistics ($\sim 1\ \sigma$) across the flux levels included in our sample. In the X-ray color-color plot, most sources fall in the location characterized by photon index = 1.5–2 and $N_{\rm H}$ = a few $\times\ 10^{20}$ cm^2, suggesting that they are typical broadline AGNs. There also exist a considerable number of sources with peculiar X-ray colors (e.g., highly absorbed, very hard, very soft). We confirm a trend that on average the X-ray color hardens as the count rate decreases. Since the hardening is confined to the softest energy band (0.3–0.9 keV), we conclude that it is most likely due to absorption. We cross-correlate the X-ray sources with other catalogs and describe their properties in terms of optical color, X-ray–to–optical luminosity ratio, and X-ray colors.

Subject headings: galaxies: active — surveys — X-rays: galaxies

On-line material: color figures

1. INTRODUCTION

The launch of the *Chandra X-Ray Observatory* has opened a new era in X-ray astronomy. With its unprecedented subarcsecond spatial resolution (van Speybroeck 1997), in conjunction with its high sensitivity and low background, *Chandra* is providing new views of the X-ray sky 10–100 times deeper than previously possible (Weisskopf et al. 2000). Indeed, the cosmic X-ray background (XRB), whose populations have long been debated because the necessary spatial resolution was lacking, is now almost ($\sim$ 80%) resolved into discrete sources in deep *Chandra* observations, e.g., the CDF-N (Chandra Deep Field–North; Brandt et al. 2001) and CDF-S (Giacconi et al. 2001). Moretti et al. (2003) have recently reported an even higher fraction ($\sim$ 90%). However, the nature of these sources is still somewhat unclear (e.g., Hasinger et al. 1998). An absorbed active galactic nucleus (AGN) population is predicted by population synthesis models (e.g., Comastri et al. 1995; Gilli, Rosati, & Salvati 1999) since the cosmic XRB is much harder (a photon index of $\sim$ 1.4) than typical AGNs, which have a photon index of $\sim$ 1.7 (e.g., Marshall et al. 1980; Fabian & Barcons 1992). There is some observational evidence supporting the existence of red, absorbed quasars (e.g., Kim & Elvis 1999; Wilkes et al. 2002; White et al. 2003). However, the hard sources in the deep surveys appear to be a mix of various types of narrow- and broadline AGNs and apparently normal galaxies, with very few of the expected type 2 AGNs seen. The statistical importance of these various source types requires a large sample resulting from a wider area survey, such as the *Chandra* Multiwavelength Project (ChaMP). In addition, with two highly successful X-ray observatories currently in orbit (*Chandra* and *XMM-Newton*), we will soon be able to address such fundamental questions as whether the density and luminosity of quasars are evolving in time (e.g., Miyaji, Hasinger, & Schmidt 2000; Cowie et al. 2003) and how clusters of galaxies form and evolve (e.g., Rosati et al. 2002). We will also discover whether rare but important objects have been missing from previous studies (e.g., the blank-field sources discussed in Cagnoni et al. 2002).

To take full advantage of the rich data set available in the *Chandra* public archive, we have initiated a serendipitous X-ray source survey, the ChaMP. Owing to the high spatial resolution, the identification of X-ray sources is far less ambiguous than in previous missions, where many counterparts were often found within typical error circles (at least $\sim$10 times larger). Additional information and artificial selection criteria are no longer required, leaving little bias. The ChaMP, although not as deep as the CDFs, covers a wide area ($\sim$14 deg^2) and can provide an order of magnitude more sources at intermediate flux levels ($F_{\rm X} \sim 10^{-14}$ to 10^{-15} ergs s^{-1} cm^{-2}) than either the CDF surveys or the previous missions (see Fig. 1 in Kim et al. 2004, hereafter Paper I). An additional advantage of a wide-area survey is the ability to investigate field-to-field variations of the number density of cosmic (background) sources, which may trace filaments and voids in the underlying large-scale structure or, if not detected, constrain the hierarchical structure formation.

In Paper I we describe our data reduction and analysis methods uniquely developed for this project and present the first catalog obtained with an initial sample of 62 *Chandra* observations. In this paper we present the results of X-ray source properties by producing the $\log N{-}\log S$ relation and X-ray colors and by comparing with data at other wavelengths. In an accompanying paper (Green et al. 2004), we present the first results of deep optical follow-up observations.

This paper is organized as follows. In § 2 we briefly describe our data reduction and analysis methods. In § 3 we present the number-flux relation, or $\log N{-}\log S$, and test its variation between different samples and from one field to another. In § 4 we discuss spectral properties of X-ray sources with X-ray colors. In § 5 we compare with data at other wavelengths, and in § 6 we present our conclusions.

2. ChaMP X-RAY DATA

Data selection and reduction processes are described in detail in Paper I. Here we present a brief summary. We have carefully selected 137 *Chandra* fields that are best suited for ChaMP science. We have applied a ChaMP-specific pipeline (called XPIPE) to uniformly reduce the *Chandra* data and to generate homogeneous data products. XPIPE was built mainly with CIAO (ver. 2.3) tools.[1] It consists of screening bad data, correcting instrumental effects, detecting X-ray sources (with *wavdetect*), and determining source properties (including photometric, spectral, spatial, and temporal information). We have also performed a large set of simulations to quantitatively assess the source validity and positional uncertainty of *wavdetect*-detected sources (see Paper I for detailed descriptions and results). The ChaMP-selected energy bands and the definition of X-ray colors are listed in Table 1.

Sixty-two fields (see Table 1 in Paper I) have been completed in XPIPE processing and follow-up manual verification and validation. We have found 4517 sources, after excluding false sources (such as detections due to bad pixels/columns; see Table 3 in Paper I). Further excluding the target of each observation, sources at the edges of CCDs, and sources affected by pileup (in our 62 fields they all happened to be targets), we end up with 4005 sources; 3177 sources are within CCDID = 0–3 in ACIS-I observations and CCDID = 6–7 in ACIS-S observations.

3. $\log N{-}\log S$

3.1. *Constructing* $\log N{-}\log S$

The cumulative surface number density versus flux relation, or $\log N{-}\log S$, has been extensively used in understanding the nature of the cosmic XRB and AGN populations and their evolution (e.g., Hasinger et al. 1993). CDF surveys have now resolved almost all the XRB (Mushotzky et al. 2000; Giacconi et al. 2001; Brandt et al. 2001); however, they cover only limited sky area. The advantage of wide-area surveys such as the ChaMP lies in finding a large number of sources (including rare objects) at intermediate to high fluxes. In particular, the ChaMP sources nicely cover the gap between the wide but shallow *ROSAT*/*ASCA* data and the deep but narrow CDF data. Another important advantage of the ChaMP is the ability to address any systematic field-to-field cosmic variations, for example, to confirm the reported overdensity of background sources near X-ray clusters (e.g., Cappi et al. 2001).

To compare with the existing data, we have made our $\log N{-}\log S$ plots in the soft band (0.5–2.0 keV) and in the hard band (2–8 keV), following the convention widely used in the literature. Since they are similar to our S and H energy bands (see Table 1), we convert the count rates determined in our S and H bands to the flux in the above two energy bands. To calculate energy conversion factors (ECFs), we assume a power-law emission model of $\Gamma_{\rm ph} = 1.7$ for the soft band and $\Gamma_{\rm ph} = 1.4$ for the hard band, with absorption by Galactic $N_{\rm H}$ determined for each observation (Stark et al. 1992). Those parameters were selected to be consistent with other results (e.g., Hasinger et al. 1993; Brandt et al. 2001) for direct comparison. As described in Paper I, the time-dependent quantum efficiency (QE) degradation is corrected for each observation. We note that the S-band ECF varies by about 20% (for about 20 months spanning our sample) because of QE degradation, while the H-band ECF remains almost constant.

To construct the $\log N{-}\log S$ relation, we have started with sources of reliable quality (i.e., 3177 sources). Completeness (as well as the Eddington bias) could still affect the result considerably at the fainter end of $\log N{-}\log S$. As seen in Figure 9 in Paper I, the detection probability is a function of source counts as well as off-axis distance. Therefore, we have included only sources that are (1) bright (more than 20 soft-band counts for the soft-band $\log N{-}\log S$ and more than 20 hard-band counts for the hard-band $\log N{-}\log S$) and (2) nearly on-axis ($D_{\rm off\text{-}axis} < 400''$ in ACIS-I observations or detected only on CCDID = 7 in ACIS-S observations). These strict selection criteria ensure the completeness of our sample (>95%), now with 707 and 236 sources in the S and H bands, respectively. We note that we do not exclude those extreme sources that are detected in only one energy band. Utilizing the full data set would bring the $\log N{-}\log S$ relation down to an order of magnitude lower flux level. However, that requires careful, complex correction for incompleteness (e.g., Vikhlinin et al. 1995; Kenter & Murray 2003), and we will present the detailed study with full corrections in a subsequent paper. All the X-ray sources used in this study are included in the first ChaMP catalog (Paper I).

First, we have determined the sky area coverage as a function of limiting flux. The limiting flux is calculated (per chip per energy band) for a source with 20 counts in a given effective exposure time. The sky area is calculated with the

TABLE 1

ENERGY BANDS AND DEFINITION OF X-RAY COLORS

Term	Definition
Energy-Band Selection	
Broad (B)	0.3–8.0 keV
Hard (H)	2.5–8.0 keV
Soft (S)	0.3–2.5 keV
Soft 1 (S_1)	0.3–0.9 keV
Soft 2 (S_2)	0.9–2.5 keV
Hardness Ratio and X-Ray Colors	
HR	$(H - S)/(H + S)$
C21	$-\log S_2 + \log S_1 = \log(S_1/S_2)$
C32	$-\log H + \log S_2 = \log(S_2/H)$

---

[1] See http://cxc.harvard.edu/ciao.

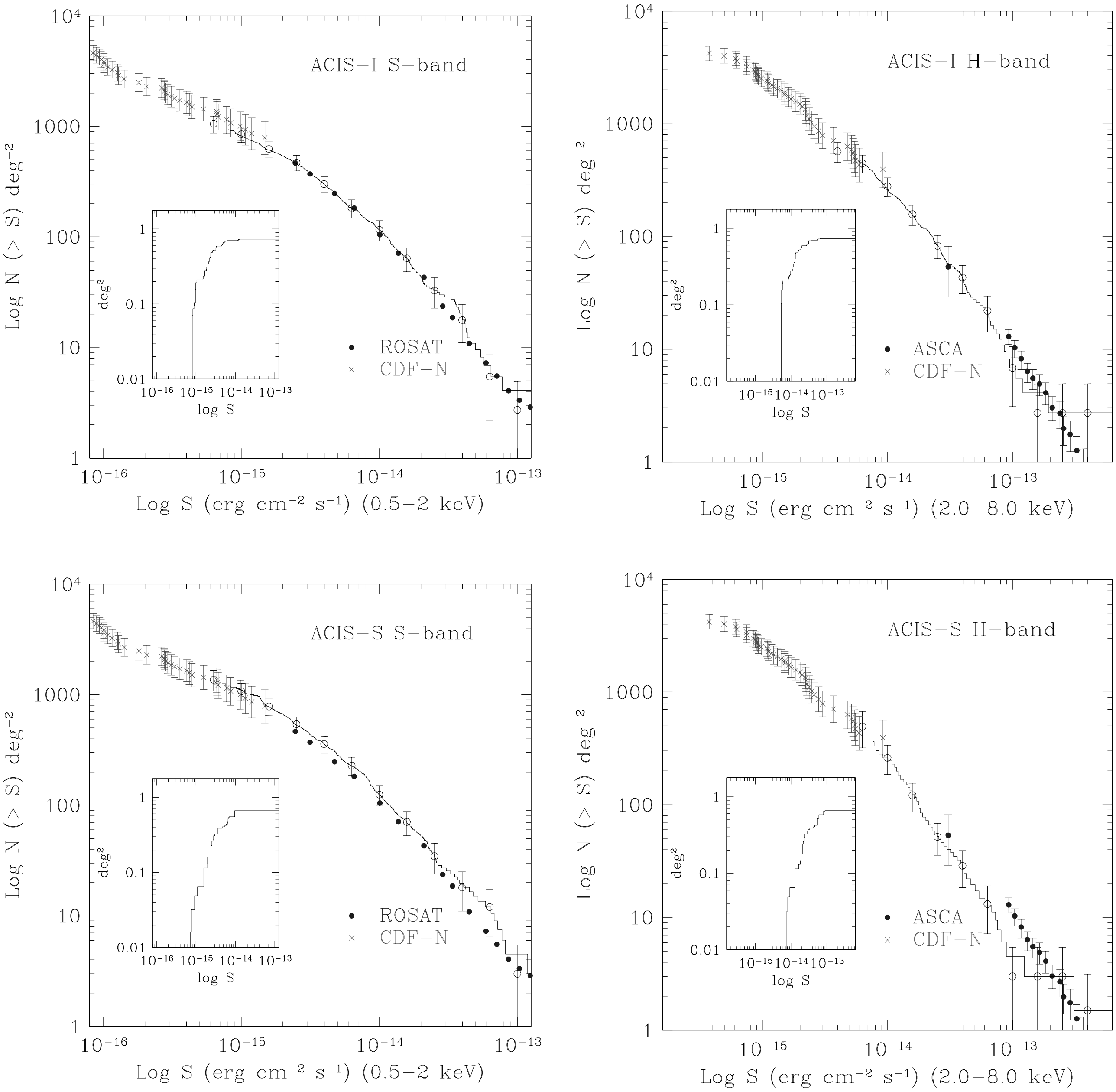

FIG. 1.—The $\log N - \log S$ plot in the soft energy band (0.5–2 keV; *left*) and in the hard band (2.0–8.0 keV; *right*), measured separately in ACIS-I (CCDID = 0–3; *top*) and ACIS-S (CCDID = 7; *bottom*). The solid histogram and open circles with error bars are our unbinned and binned data, respectively. Also plotted for comparison are results from the Hubble Deep Field–North and previous missions (*ROSAT* in the S band and *ASCA* data in the H band). [*See the electronic edition of the Journal for a color version of this figure.*]

geometrical area (per chip) after correcting for interchip gaps and for the 10% exposure threshold, which we have applied in XPIPE to remove spurious sources (see § 3.2 in Paper I). Since we are excluding sources falling at the edge of the chip, we need to correspondingly reduce the covered sky. This correction is complicated because it varies with the source size (i.e., with the off-axis angle). Instead, we simply correct this effect by the fraction of sources at the edge. Typically, it is ∼8% in ACIS-S and ∼3% in ACIS-I.

Then, the cumulative $\log N - \log S$ relation is computed by summing up the sky-area–weighted source contribution:

$$N(>S) = \sum_{S_i > S} \frac{1}{\Omega_i} ,$$

where $N(>S)$ is the surface number density of sources with flux greater than S, S_i is the flux of the ith source, and Ω_i is the solid angle (sky-area coverage) at the flux S_i.

Figure 1 shows the cumulative $\log N - \log S$ plots, which were determined separately in ACIS-I front-illuminated (FI) CCDs (CCDID = 0–3) and the ACIS-S back-illuminated (BI) CCD (CCDID = 7). The solid histogram and open circles with error bars are our unbinned and binned data, respectively. We use only unbinned data in the following analysis but present binned data here to indicate the amount of associated errors. The results from the FI (*top*) and BI (*bottom*) chips are remarkably similar, indicating that any systematic error in count-to-flux conversion factors between FI and BI is minimal. In the S band (*left*), the $\log N - \log S$ measured with ACIS-S sources is slightly higher than that of ACIS-I, but it is fully

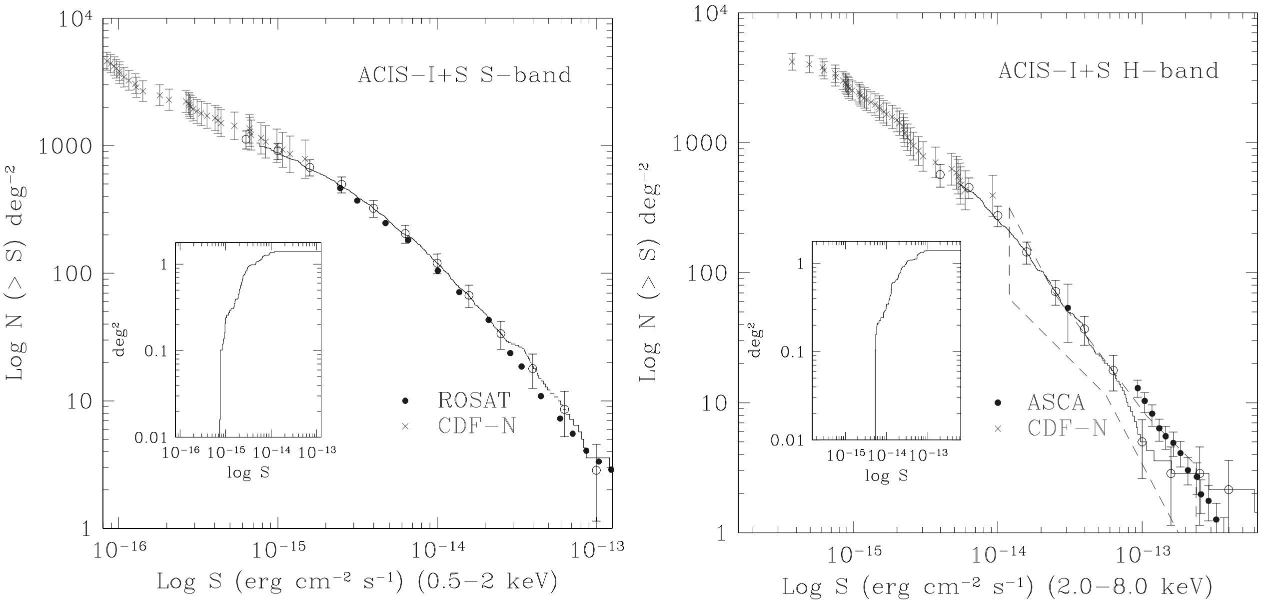

FIG. 2.—Same as Fig. 1, but with all sources detected in ACIS-I and ACIS-S. The dashed line (*right*) indicates the results of the *ASCA* fluctuation analysis. [*See the electronic edition of the Journal for a color version of this figure.*]

consistent within a statistical error of 1 σ. In the H band (*right*), the trend is opposite. ACIS-S data points are slightly lower than those of ACIS-I. Again the difference is not statistically significant, even less significant than that in the S band. In Figure 2, we plot the $\log N - \log S$ relation determined with combined FI and BI data and compare with previous results. In the S band, the CDF-N (Brandt et al. 2001) and *ROSAT* (Hasinger et al. 1993) data are marked by crosses and filled circles, respectively. Similarly, in the H band, the CDF-N (Brandt et al. 2001) and *ASCA* (Ueda et al. 1998; Ogasaka et al. 1998; converted to $\Gamma_{\rm ph} = 1.4$) data are marked by crosses and filled circles. The *ASCA* fluctuation analysis result (*blue bow tie*) by Gendreau, Barcons, & Fabian (1998) is also plotted. In both the S and the H bands, our data are consistent with the previous results, down to 8×10^{-16} and 5×10^{-15} ergs s^{-1} cm^{-2} for the S and H bands, respectively. Our H-band data fill the large flux gap between the CDF-N and *ASCA* data. Our H-band data point is slightly lower at the high-flux end ($S = 10^{-13}$ ergs cm^{-2} s^{-1}) than the *ASCA* data (Ueda et al. 1998). The *ASCA* fluctuation analysis result (Gendreau et al. 1998) appears to be consistent with our data, suggesting the same trend. However, the difference is only marginally significant (<2 σ). With the full ChaMP sample, we will be able to confirm whether there is any statistically significant difference. Although we do not plot the CDF-S data (Giacconi et al. 2001; Rosati et al. 2002), they are consistent with the CDF-N where they overlap with our data (see below for further discussion).

In the S band, the slope starts to flatten at $\sim 10^{-14}$ ergs s^{-1} cm^{-2}, as noted in the *ROSAT* (Hasinger et al. 1998) and *XMM* data (Baldi et al. 2002). Using the maximum likelihood method (Murdoch, Crawford, & Jauncey 1973), we have fitted our differential $\log N - \log S$ in the flux range of 10^{-15} to 10^{-13} ergs s^{-1} cm^{-2}. A single power-law fit is not statistically acceptable, so a broken power-law model is applied as follows:

$$\frac{dN}{dS} = \begin{cases} KS^{-\beta_{\rm bright}} & S > S_{\rm break}, \\ \left(KS_{\rm break}^{\beta_{\rm faint}-\beta_{\rm bright}}\right) S^{-\beta_{\rm faint}} & S < S_{\rm break}. \end{cases}$$

The best-fit slopes for the differential $\log N - \log S$ are $\beta_{\rm bright} = 2.2 \pm 0.2$ at the bright end and $\beta_{\rm faint} = 1.4 \pm 0.3$ at the faint end, with the break energy $S_{\rm break}$ equal to $(6 \pm 2) \times 10^{-15}$ ergs s^{-1} cm^{-2}. The normalization constant K is 2030 ± 210 when S is normalized by 10^{-15} ergs cm^{-2} s^{-1}. These are consistent with those previously determined by the *ROSAT* (Hasinger et al. 1998) and *XMM* data (Baldi et al. 2002; Hasinger et al. 2001). In particular, our results are almost identical to those of Baldi et al. (2002) obtained in a similar flux range. The CDF-N data (Brandt et al. 2001) fitted in the fainter flux range 5×10^{-17} to 2×10^{-15} ergs s^{-1} cm^{-2} resulted in a slope of the cumulative $\log N - \log S$ $\alpha = 0.67 \pm 0.14$, which is again in good agreement with our data ($\alpha = 0.7 \pm 0.15$ for a single power-law fit at $f_{\rm X} < 5 \times 10^{-15}$ ergs s^{-1} cm^{-2}; note that $\alpha = \beta - 1$ does not hold below $S_{\rm break}$). We have also fitted our H-band $\log N - \log S$ in the flux range 5×10^{-15} to 2×10^{-13} ergs s^{-1} cm^{-2}. A single power law is statistically acceptable with the best fit $\beta = 2.1 \pm 0.1$ and the normalization constant $K = 3160 \pm 250$, when S is normalized by 10^{-15} ergs cm^{-2} s^{-1}. Our result is again consistent with the *XMM* result ($\alpha = 1.34 \pm 0.1$) determined in a similar flux range by Baldi et al. (2002) and the CDF-N result ($\alpha = 1.0 \pm 0.3$) determined in a slightly fainter flux range ($F_{\rm X} > 1.5 \times 10^{-15}$ ergs s^{-1} cm^{-2}) by Brandt et al. (2001). A flattening similar to that in the S band may exist with a break around $S \sim 10^{-14}$ ergs s^{-1} cm^{-2}, which was also noticed in the *XMM* Lockman Hole deep observations (Hasinger et al. 2001).

3.2. *Is There Field-to-Field Cosmic Variation?*

Taking advantage of a large number of observational fields, we can compare source density distributions in various subsamples. In particular, Cappi et al. (2001) reported a considerable overdensity (in the S band) in two cluster fields, when compared to the source density in noncluster fields. This is intriguing because the overdensity might be caused by the presence of clusters, indicating cosmic spatial variation of number densities by enhancing AGNs or starburst galaxies associated with the clusters or gravitationally lensed sources.

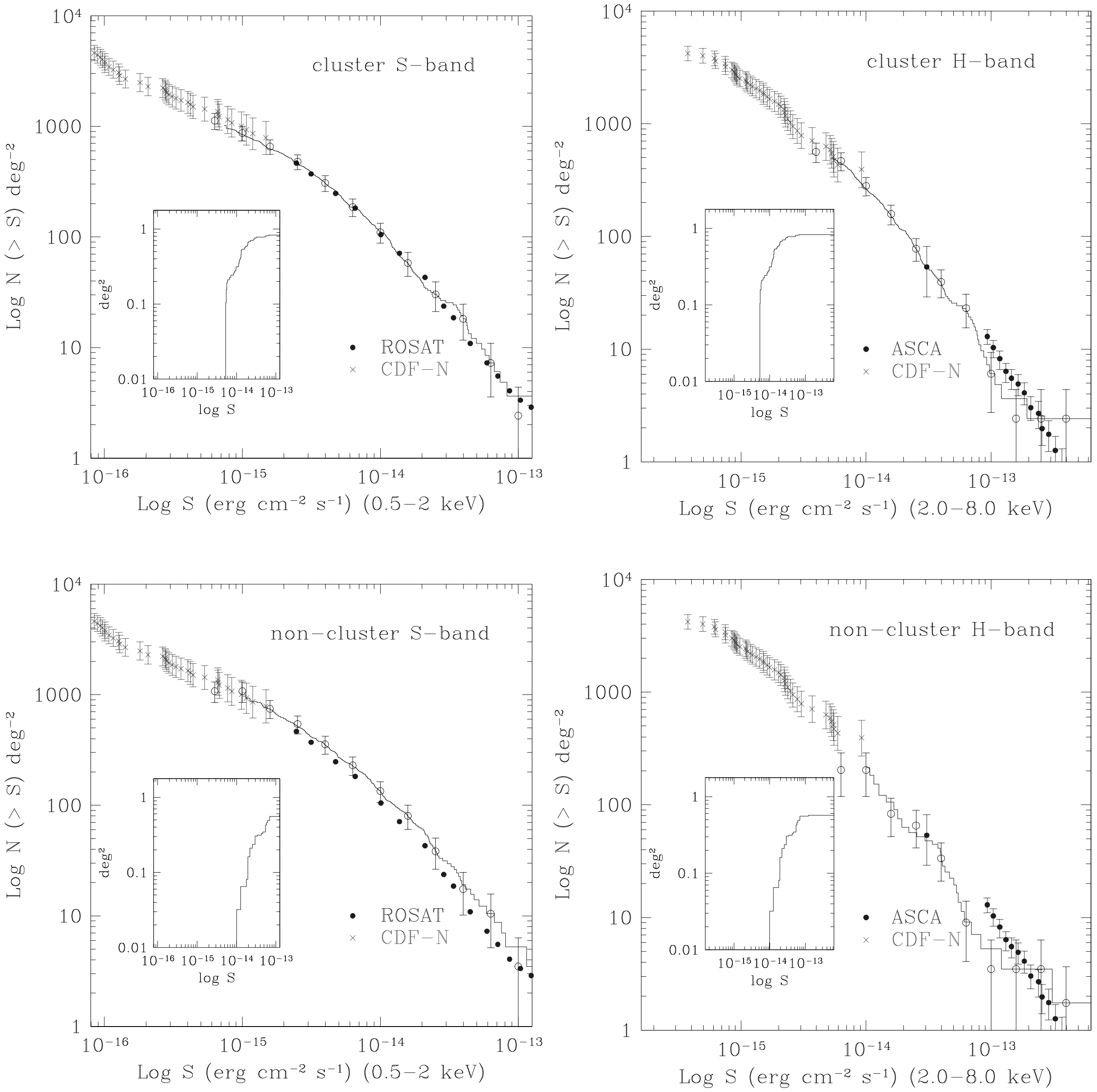

FIG. 3.—Same as Fig. 1, but made separately with sources found in the fields with (*top*) and without (*bottom*) an X-ray cluster. [*See the electronic edition of the Journal for a color version of this figure.*]

To check this possibility, we have divided the 62 observations into two groups, those containing one or more previously known X-ray clusters and the rest. We have 29 fields with clusters and 33 without clusters. We have then determined $\log N - \log S$ separately in the fields with and without X-ray clusters and plotted them in the top and bottom panels of Figure 3. There is no statistically significant difference between the results with or without the X-ray clusters. It appears that in the S band, noncluster fields may have a slightly higher density than cluster fields (i.e., opposite to what Cappi et al. found), but the difference is within a statistical error of 1 σ. We note that most observations of cluster fields were performed in ACIS-I, while most noncluster observations were in ACIS-S. The amount and sense of the difference are the same as those between ACIS-S and ACIS-I, as described above. In conclusion, the small difference (if any) could be due to the slight error in the calibration between ACIS-S and ACIS-I or to the presence or absence of clusters. If the presence of clusters makes the difference, the sense of the effect is opposite that of the previous suggestion by Cappi et al. (2001).

To further test any field-to-field variation in cosmic background source densities, we have calculated the expected number of sources based on our $\log N - \log S$ plot for a given exposure time and then compared them with the number of detected sources in each observation. As in § 3.1, we have used only sources (1) with more than 20 counts in the S or H band and (2) either within $D_{\text{off-axis}} < 400''$ for ACIS-I or in S3 for ACIS-S. In Figure 4 the ratio of detected to expected source numbers is plotted against the exposure time. Data taken from different energy bands and different CCDs are marked with different symbols and colors. Also plotted are a few typical errors with the same symbols and colors. In short-exposure observations (toward the left side of the figure), the

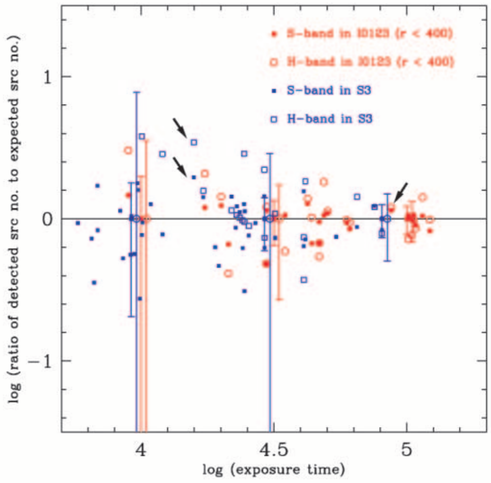

FIG. 4.—Number of detected sources compared with the number of expected sources, based on our fitted $\log N - \log S$. Filled (open) circles indicate sources detected in the S (H) bands in four ACIS-I CCDs within 400″ of the aim point. Similarly, squares are for the ACIS-S CCD (S3). Typical errors are plotted with the same symbol and color as the data points. Also, the data obtained in the 3C295 field are marked by arrows.

number of detected sources is small (typically less than 10 in 10 ks observations) and hence there is a large scatter with a correspondingly large error bar. On the other hand, in relatively long exposure observations (toward the right side of the figure), as the number of detected sources increases (typically 30–40 sources in 100 ks observations), the error is small and hence the test result is more significant. The number of detected sources is consistent with the expected number. Among a dozen data points with exposure times of $\sim$100 ks, only one (observation ID [ObsID] 536 in the H band) has a deviation larger (but only slightly) than the 1 σ error. Also marked in the figure are those data points determined in the two observations (shallow ACIS-S and much deeper ACIS-I observations) of the 3C 295 field, where Cappi et al. (2001) reported the existence of an overdensity. The deeper observation clearly excludes this possibility. V. Delia et al. (2003, in preparation) found the same result with the deeper ACIS-I observations, i.e., no excess in this field of view, but also reported a smaller scale, asymmetric distribution of X-ray sources. We will search for a scale-dependent density variation with the full ChaMP data set. We conclude that there is no indication of significant field-to-field variation in cosmic background source densities, within the statistics and over the flux levels included in our sample.

There have been some debates on whether the results from the CDF-N (Brandt et al. 2001) and CDF-S (Giacconi et al. 2001) are consistent with each other. Recently, Rosati et al. (2002) reported that they are consistent within 2 σ at the faint end (also consistent with our result), whereas the CDF-S contains a significantly lower number of sources at bright fluxes. We note that the source density in the CDF-S ($N \sim 680 \pm 150$ deg^{-2}; Rosati et al. 2002) is consistent within $\sim$1 σ with that in the CDF-N ($N \sim 930 \pm 300$ deg^{-2}; Brandt et al. 2001) at $f_X = 10^{-15}$ ergs s^{-1} cm^{-2} (in the S band), where our data overlap with the CDF-N data (see Fig. 2). At bright fluxes, there are only a small number of sources in both CDFs. At $f_X \sim 8 \times 10^{-14}$ ergs s^{-1} cm^{-2} (in the S band), where the discrepancy appears largest, there are only about five real sources (with $N \sim 70$ deg^{-2}) in the CDF-S. At the same flux limit, our sample has $\sim$200 sources and hence carries much better statistics and provides a robust determination of the source density. Recently, Yang et al. (2003) reported a field-to-field variation (mostly in the H band) from the contiguous Lockman Hole NW covering 0.33 deg^2, while the $\log N - \log S$ relation from the entire field is consistent with that of the CDF-N. However, it is not clear why the clustering is significant only in the H band but not in the S band, where the statistics are higher ($\sim$3 times more sources in the S band). This requires further confirmation.

To test whether there is any systematic difference between fields with high and low Galactic $N_{\rm H}$ (or equivalently high and low Galactic latitude), we have again divided our sample into two groups with $N_{\rm H}$ higher or lower than 3×10^{20} cm^{-2}. Again, we do not see any systematic difference (note that we applied ECF as a function of $N_{\rm H}$).

4. X-RAY COLORS

4.1. *Constructing X-Ray Colors*

X-ray colors can be used to determine average spectral properties of a given sample of sources, which are not sufficiently bright to allow individual spectral fitting. We have developed two X-ray colors as defined in Table 1 to determine intrinsic spectral hardness and absorption. These colors are defined according to the convention used in optical colors: a large number in X-ray colors means a red (i.e., soft) spectrum. As in § 3, we have started with those sources of good quality (i.e., 3177 sources) but then limited ourselves to only sources with more than 50 net counts in the *B* band in CCDID = 0–3 in ACIS-I and CCDID = 6–7 in ACIS-S observations. We note that we include those sources that are not detected in all energy bands (they will have upper/lower limits in X-ray colors). Figure 5 shows the distribution of the resulting 620

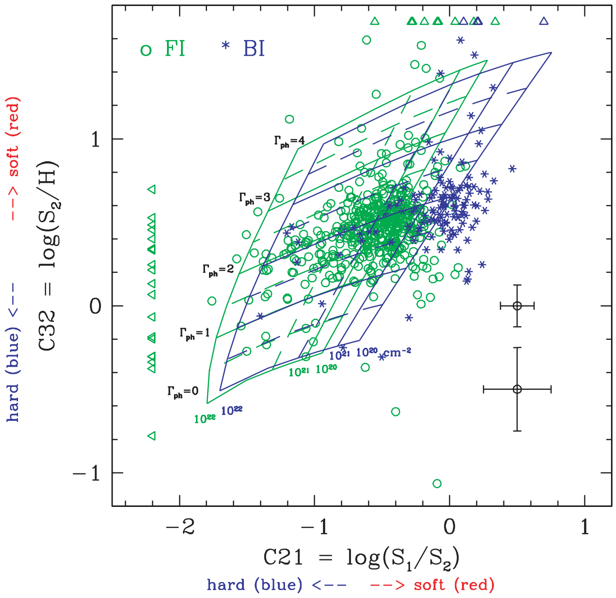

FIG. 5.—X-ray color-color plot. X-ray colors, C21 and C32, are defined as in Table 1. The sources detected with more than 50 counts in FI and BI chips are marked by green circles and blue stars, respectively. The upper limits of X-ray colors for sources detected in only one band are marked by triangles at the top and on the far left. The green (FI) and blue (BI) grids indicate the location of predicted X-ray colors of power-law spectra with specified parameters. The two error bars in the lower right corner represent typical errors for sources with 50 and 100 net counts.

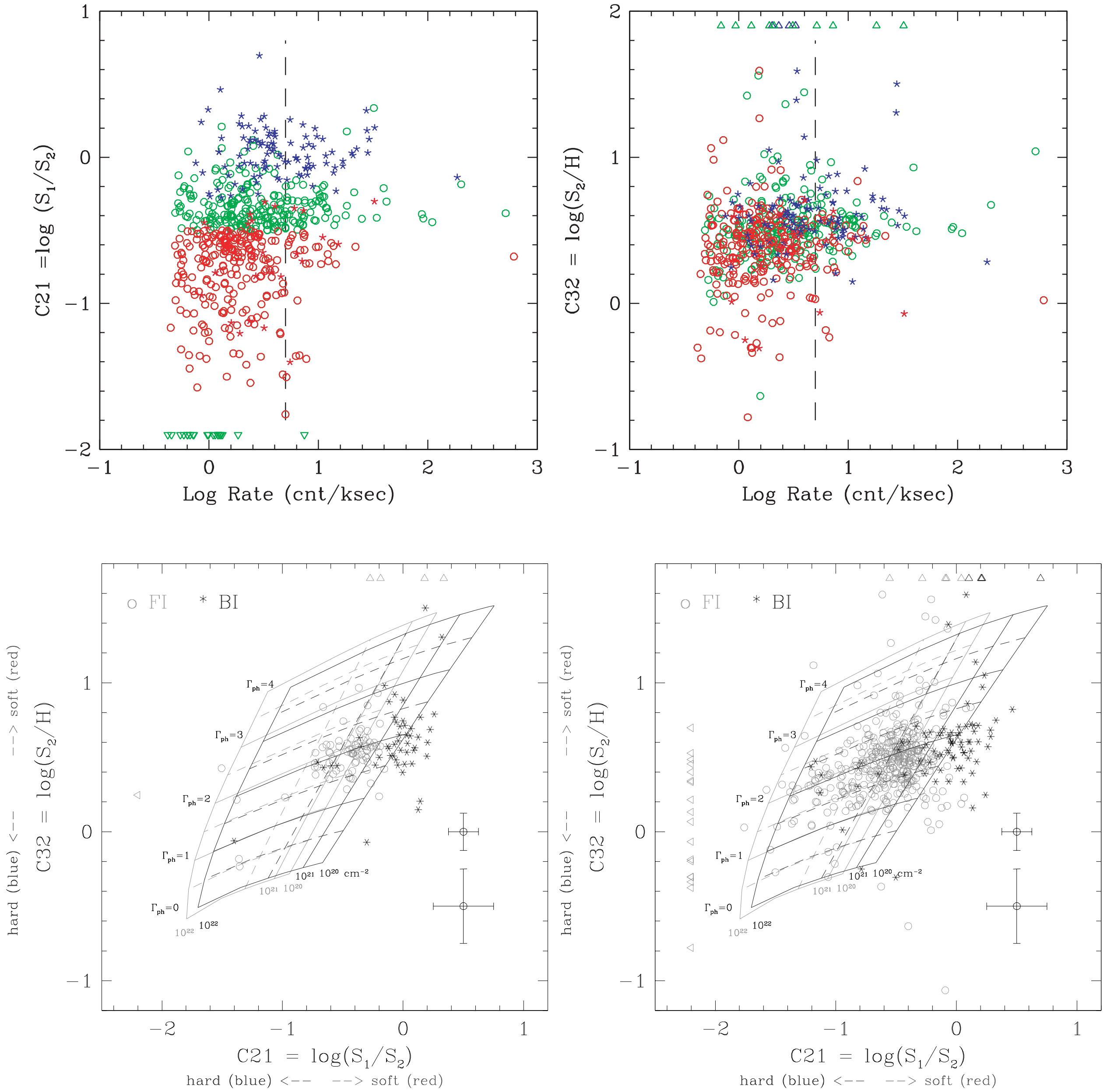

FIG. 6.—(*a, b*) X-ray colors as a function of X-ray count rate in *B* band. The color code is the same as in Fig. 5, except that absorbed sources with C21 < -0.5 for FI (or C21 < -0.3 for BI) are marked by red circles (or stars). (*c, d*) Same as in Fig. 5, except sources with net count rate in *B* band higher (*c*) and lower (*d*) than 5 counts ks^{-1} (*vertical dashed lines in [a] and [b]*) are plotted separately. [*See the electronic edition of the Journal for a color version of (c) and (d).*]

sources in the X-ray color-color plane. All the X-ray sources used in this study are included in the first ChaMP catalog (Paper I). Sources from FI chips are plotted as green circles and sources from BI chips as blue stars. Also plotted are error bars representative for sources with 50 and 100 net counts with a typical spectrum ($\Gamma_{\mathrm{ph}} = 1.7$ and $N_{\mathrm{H}} = 3 \times 10^{20}$ cm^{-2}). Note that those sources detected only in one band are marked with triangles pointing toward the appropriate direction in the color-color plane, i.e., at the top (no detection in H band) or at the far left (no detection in S_1 band).

The grid in the X-ray color-color plot (Fig. 5) indicates the predicted locations of local sources at $z = 0$ with various photon indexes (Γ_{ph} ranging from 0 to 4) and absorption column densities (N_{H} ranging from 10^{20} to 10^{22} cm^{-2}). Note that C21 depends mostly on absorption (which changes X-ray colors horizontally), whereas C32 depends on intrinsic spectral hardness (which changes vertically). Because ACIS-S is more sensitive in the lower energies ($E < 1$ keV, or mostly in our S_1 band) than ACIS-I, the QE difference in two CCDs affects mostly C21 and the ACIS-S grid shifts to the right. The model prediction appropriate for ACIS-I is in green, while that for ACIS-S is in blue, applying the same colors as the sources. As described in § 3, the model grid varies as a function of observation date, because of the ACIS QE degradation. X-ray colors of a typical source with $\Gamma_{\mathrm{ph}} = 1.7$ and $N_{\mathrm{H}} = 3 \times 10^{20}$ cm^{-2}, which would have obtained in the earliest and latest observations (spanning about 20 months), differ by ~ 0.15 in C21 (much smaller in C32, ~ 0.02). This amount of ΔC21 is comparable to the error of typical sources with 100 counts (see Fig. 5). The grids plotted in Figure 5 were made with ObsIDs 00615 (for ACIS-S) and 00926 (for ACIS-I), which were observed near the midpoint of the 20

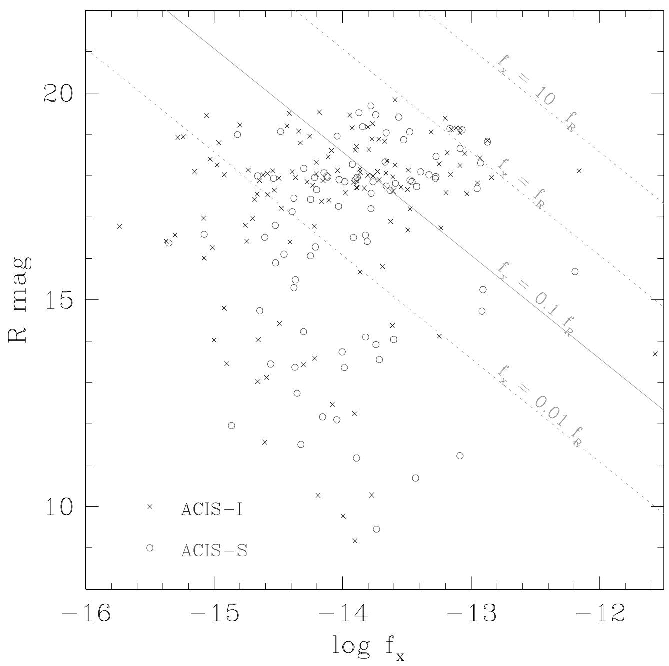

FIG. 7.—X-ray sources with USNO optical counterparts. The X-ray flux is determined in the 0.5–2.0 keV band, and the X-ray–to–optical flux ratio is given by $\log f_X/f_R = \log f_X + 5.57 + R/2.5$. The upper right corner (i.e., $f_X > 0.1f_R$; *green line*) is mainly occupied by quasars, whereas the lower left corner (i.e., $f_X < 0.1f_R$) is primarily occupied by local stars and galaxies, as determined in the EMSS and ChaMP (see also Green et al. 2004). [*See the electronic edition of the Journal for a color version of this figure.*]

month span of our sample on 2000 July 10–11 (see Table 1 in Paper I). The X-ray colors are not corrected for vignetting, because the difference in the effective area at the off-axis angle of 10″ between energies of 1.496 and 4.510 keV is only ∼5% (see Chandra X-Ray Center 2000), or ∼0.01 in X-ray colors, which is much smaller than the typical errors.

From Figure 5 it is clear that sources are concentrated at the location of typical broadline AGNs with small intrinsic absorption, i.e., around $G_{\rm ph} = 1.5$–2 and $N_{\rm H}$ = a few × 10^{20} cm^{-2}. About 70% of the sources in Figure 5 are, within statistical errors, consistent with being a typical broadline AGN. However, there are a considerable number of outliers, which could consist of rare, interesting sources such as highly absorbed, very soft, or very hard sources. For example, the source at the bottom of Figure 5 (with C32 = −1.06), CXOMP J114147.9−660604, is a very hard source with almost all X-rays falling in the H band (note that C21 is very uncertain because of the small number of counts in $E < 2.5$ keV). This corresponds to $\Gamma_{\rm ph} \leq -2$ if a significant amount of intrinsic absorption is absent. On the other hand, if this is due to absorption, $N_{\rm H} \geq 10^{23}$ cm^{-2} is required for a typical power-law spectrum with $\Gamma_{\rm ph} = 1.5$–2. Since no sources with $\Gamma_{\rm ph} \leq -2$ are known to exist, this source is likely a heavily absorbed AGN. Optical imaging data (Green et al. 2004; optical spectroscopy will be obtained in the summer of 2003) also imply that it is optically a very red object, with g'–$i' > 4.8$ (or g'–$r' > 3.4$). With $r' = 21.9$ mag, its X-ray–to–optical flux ratio is $f_X/f_r \sim 1.0$, which is typical for AGNs (see Figs. 7 and 8). There are several very soft sources at the top of Figure 5 (C32 ≥ 1.4), corresponding to $G_{\rm ph} \geq 4$. Some of them could be X-ray stars (see Fig. 9). Also present are several absorbed sources at the far left of Figure 5, corresponding to absorption by $N_{\rm H} \geq 10^{22}$ cm^{-2}. We expect to collect an order of magnitude more of these unusual sources in the full ChaMP sample. As follow-up optical imaging and spectroscopic observations progress (Green et al. 2004), we will be able to determine the nature of these peculiar sources.

4.2. *X-Ray Color Variation*

Since the XRB spectrum is harder than that of typical quasars (e.g., Gursky & Schwartz 1977), it has been suggested that the average source spectra would be harder with decreasing source fluxes (e.g., Comastri et al. 1995; Gilli et al. 1999). Recent observational data obtained by *Chandra* and *XMM* also support spectral hardening (e.g., Hasinger et al. 2001; Alexander et al. 2002). They could consist of type 2 quasars (Webster et al. 1995) or red quasars (e.g., Kim & Elvis 1999; White et al. 2003). It is very important to confirm or reject this trend. Another equally interesting question is whether the hardening is caused by the reduction of soft X-rays due to the increasing amount of absorption or by the enhancement of hard X-rays due to intrinsic hardening. We can test this hypothesis by comparing the average X-ray colors of sources with different X-ray fluxes. Because the absorption affects C21 more than C32, we do not expect a trend in C32 similar to that in C21 if the hardening is by the variable absorption of similar intrinsic spectra. On the other hand, if C32 exhibits a similar trend, i.e., harder colors with decreasing fluxes, then fainter sources could be intrinsically hard in X-rays.

In Figures 6*a* and 6*b*, C21 and C32 are plotted against count rates. There is a clear trend in C21 (Fig. 6*a*) such that sources with hard C21 colors appear to be X-ray–faint, while X-ray–bright sources have all soft C21 colors. In other words, the

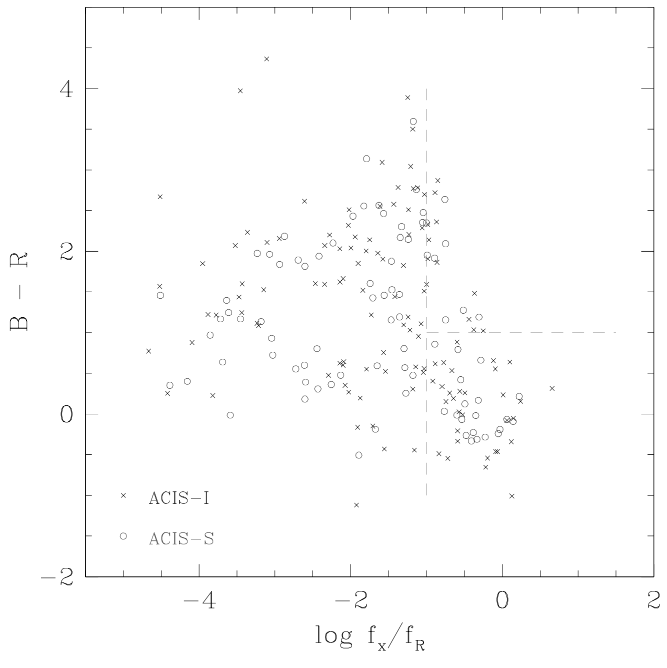

FIG. 8.—Optical colors are plotted against X-ray–to–optical flux ratio. The X-ray and *R*-band fluxes are determined as in Fig. 7. The vertical dotted line corresponds to $f_X = 0.1f_R$, so the area on the right side of that line is the location for quasars. The typical blue quasars have $B-R < 1$ (i.e., below the horizontal dotted line), whereas the absorbed, red quasars would fall above the line with $B-R > 1$, as determined in Kim & Elvis (1999) and also in the ChaMP (Green et al. 2004). [*See the electronic edition of the Journal for a color version of this figure.*]

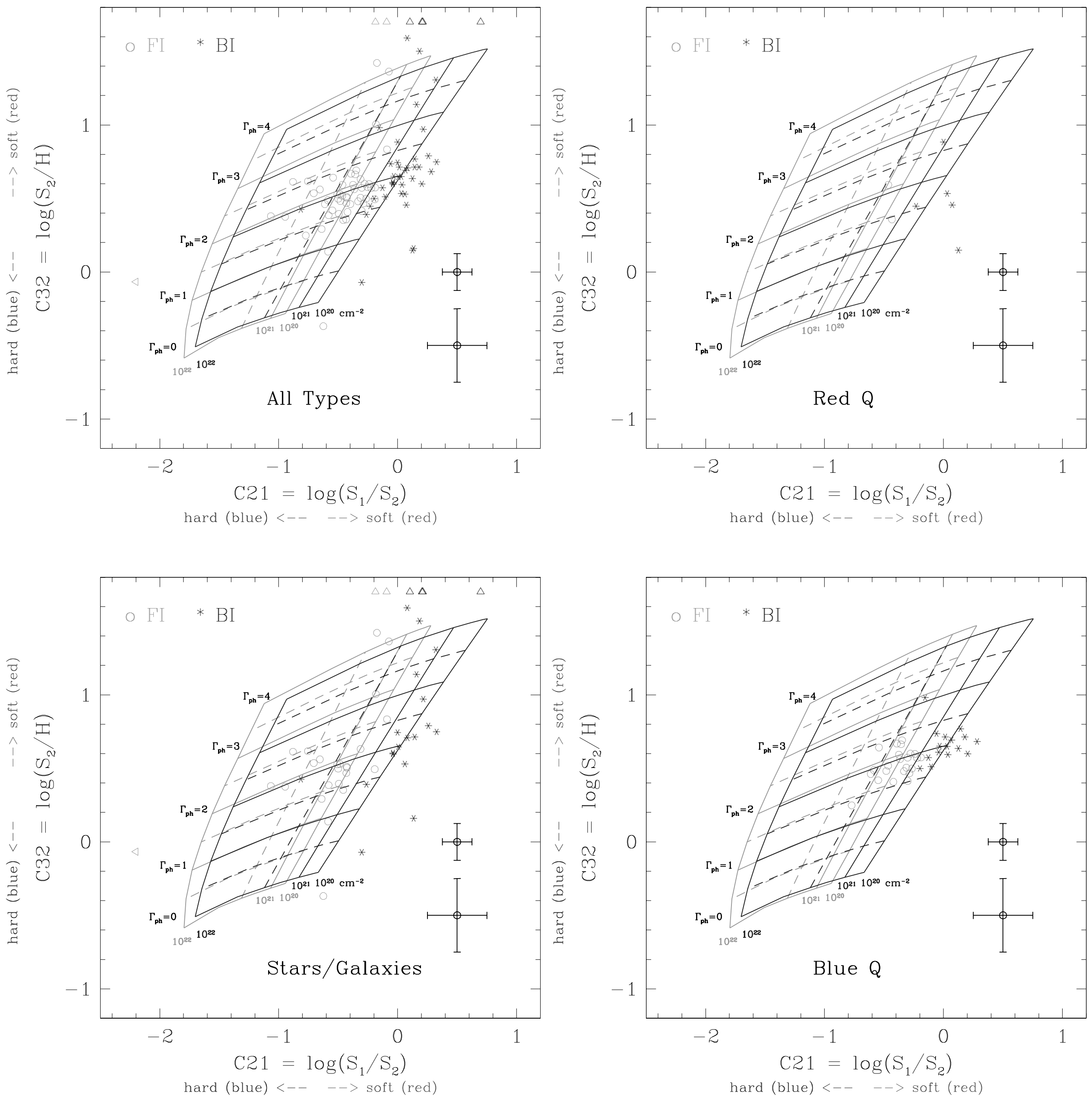

All Types

Red Q

Stars/Galaxies

Blue Q

FIG. 9.—X-ray color-color diagram. Same as in Fig. 5. (*a*) All X-ray sources with USNO optical counterparts. (*b*) Sources (possibly red quasars) in the upper right corner of Fig. 8 (i.e., $B-R > 1$ and $f_X > 0.1 f_R$). (*c*) Sources (stars/galaxies) on the left side of Fig. 8. (*d*) Sources (blue quasars) in the lower right corner of Fig. 8. [*See the electronic edition of the Journal for a color version of this figure.*]

lower right corner of Figure 6*a* is almost empty. We ran a K-S (Kolmogorov-Smirnov) test on two subgroups with X-ray *B*-band count rates higher or lower than 5 counts ks^{-1} (the vertical lines in Figs. 6*a* and 6*b* indicate this count rate). The probability that the X-ray–bright and X-ray–faint samples originate from the same parent population is $\sim 10^{-5}$, indicating that the trend in the C21 color is statistically significant. To further illustrate this, we separately plot them in the color-color diagram (Figs. 6*c* and 6*d*). The location for $N_{\rm H} > 3 \times 10^{21}$ cm^{-2} (i.e., the area to the left of the dashed line between the two solid lines indicating $N_{\rm H} = 10^{21}$ and 10^{22}) is almost empty for X-ray–bright sources (Fig. 6*c*), whereas the same space is occupied by many X-ray–faint sources (Fig. 6*d*). This is in good agreement with the expectation from the hard XRB spectra in that the faint sources (which could consist of a large part of XRB but are mostly undetected so far) are indeed more absorbed and hence harder.

In C32 the trend is much less clear. In Figure 6*a*, the hard X-ray sources with C21 < -0.5 found in FI chips (or C21 < -0.3 in BI chips, considering the higher response of BI at lower energies) are color coded with red. The same objects are also marked in red in Figure 6*b*, where C32 is plotted against the X-ray count rate. While the hard X-ray sources are clearly distinguishable in C21, they are all mixed with soft X-ray sources in C32. Likewise, the faint sources found on the left side of the color-color plane in Figure 6*c* ($N_{\rm H} > 3 \times 10^{21}$ cm^{-2}) have a distribution across the $\Gamma_{\rm ph}$ grids similar to the sources on the right side ($N_{\rm H} < 3 \times 10^{21}$ cm^{-2}); i.e., they are concentrated around the location with $\Gamma_{\rm ph} = 1.5$–2 with some scatter, but without a clear preference toward higher or lower $\Gamma_{\rm ph}$. The K-S test resulted in a much higher probability of the two data sets being drawn from the same population ($\sim 10^{-2}$) than that for C21. The absence of any systematic trend in C32 is consistent with the results in Green et al. (2004), where a single hardness ratio was used (i.e., compared counts in the S [$=S_1 + S_2$] band and in the H band). This implies that the spectral hardening of faint sources is mostly due to absorption that affects the lowest energies (thus the C21 color) and that the intrinsic spectral shape on average does not change with decreasing X-ray flux.

We note that with the chosen energy bands (§ 2) and the given sample selection (above in this section), we have upper limits in C21 (for sources detected in the S_2 band but not detected in the S_1 band) but no lower limits. On the other hand, we have lower limits in C32 (for sources detected in the S_2 band but not detected in the H band) but no upper limits. Including the upper/lower limits would add more *hard* sources (mainly to the X-ray–faint subgroup) in the C21-f_X relationship and more *soft* sources in the C32-f_X relationship. In both cases, this would slightly enhance (but not reduce) our conclusions concerning the presence/absence of the correlation of C21/C32 with f_X.

5. CROSS-CORRELATION WITH OTHER CATALOGS

With *Chandra*'s superb spatial resolution, the typical error in absolute position is $1''$ or less,[2] and the relative error of *wavdetect*-determined positions is less than $1''$–$2''$ within $D_{\text{off-axis}} < 400''$ (see § 5 in Paper I). This makes an error box at least an order of magnitude smaller than those typical of previous missions.[3] Cross-correlation with existing catalogs in other wavelengths is now substantially more reliable and without ambiguity.

As in §§ 3 and 4, we have selected only sources of good quality (i.e., 3177 sources) but have further limited ourselves to X-ray sources with good positional accuracy by applying (1) a net count in the *B* band of greater than 10 and (2) $D_{\text{off-axis}} < 400''$ regardless of ACIS-I or ACIS-S observations. Then we have cross-correlated our data with optical (USNO-A2.0; Monet et al. 1998), near-IR (Two Micron All Sky Survey [2MASS]; Cutri et al. 2000), and radio (NVSS [Condon et al. 1998] and FIRST [White et al. 1997]) catalogs, with a $3''$ search radius. We have found 207, 75, and 16 sources with USNO, 2MASS, and NVSS+FIRST counterparts, respectively. Here we concentrate on the correlation with the USNO catalog; the other results (and with the full ChaMP data set) will be presented in a separate paper.

In Figure 7, 207 sources with USNO optical counterparts are plotted in the f_X-R plane. The X-ray flux is determined in 0.5–2.0 keV, and the X-ray–to–optical flux ratio is given by $\log f_X/f_R = \log f_X + 5.57 + R/2.5$ [taken from Maccacaro et al. 1988, assuming $B-R = 1.0$ mag and $V = (B+R)/2.0$]. Also plotted are diagonal lines indicating $f_X/f_R = 0.01$–10. As determined in the Extended Medium-Sensitivity Survey (EMSS; Maccacaro et al. 1988) and also confirmed by the ChaMP (Green et al. 2004), the upper right corner (i.e., $f_X > 0.1 f_R$) is mainly occupied by quasars whereas the lower left corner (i.e., $f_X < 0.1 f_R$) is for Galactic stars and galaxies (including both narrow emission line galaxies and absorption line galaxies). This figure can be directly compared with ChaMP optical results (e.g., Green et al. 2004), where the CCD-determined optical magnitude goes much deeper ($r' \sim 24$ mag). Note that those with USNO IDs are only $\sim$10% of the sources cross-correlated in this section. Since stars and galaxies are brighter in R for a given f_X than are quasars, the relatively bright optical limit of USNO gives a biased fraction of stars and galaxies, which will change as we go fainter in R.

In Figure 8 optical colors are plotted against X-ray–to–optical flux ratio. The X-ray and R-band fluxes and their ratios are determined as in Figure 7. Again this figure can be directly compared with a similar plot in Green et al. (2004). The vertical dashed line corresponds to $f_X = 0.1 f_R$, so the area to the right of the line is the location for quasars. As seen in Green et al. (2004), the typical blue quasars have $B-R < 1$ (i.e., below the horizontal dashed line). In Figure 8 we see a concentration of typical blue quasars in the lower right region, defined by $f_X > 0.1 f_R$ and $B-R < 1.0$ mag. The area to the left of the vertical lines is the location for Galactic stars and galaxies, while absorbed red quasars or type 2 quasars would fall in the upper right corner, defined by $f_X > 0.1 f_R$ and $B-R > 1.0$ mag. Thus, the (f_X/f_R, $B-R$)-plane can be divided into three subregions hosting blue quasars (*lower right*), red quasars (*upper right*), and stars/galaxies (*left*). Using X-ray colors, we determine average X-ray spectral properties of sources falling in these three subregions. X-ray color-color diagrams for each subsample (with net counts greater than 50 as in Fig. 5) are shown in Figure 9. The blue quasars and stars/galaxies occupy different regions of the X-ray color-color diagram. The blue quasars are clearly concentrated in the region for $\Gamma_{\text{ph}} = 1.5$–2 and $N_H =$ a few $\times 10^{20}$ cm^{-2}. On the other hand, stars/galaxies are widely spread out, particularly occupying a region with higher (or softer) C32 color $\geq$ 1.0, which corresponds to $\Gamma_{\text{ph}} \geq 3$. We note that for a thermal gas model the region with C32 $\geq$ 1.0 corresponds to $kT \leq$ 1.5 keV, which is typical for galaxies and groups of galaxies. We do not have many objects in the region of red quasars (with more than 50 X-ray net counts) in our sample to draw any characteristic signature using the X-ray colors. However, they appear to spread out, contrary to the concentrated distribution of blue quasars. The full ChaMP sample with deep optical imaging data supplemented will allow us to revisit this important issue of the existence, fractions, and properties of red and/or absorbed quasars.

Among the $\sim$ 1900 sources with no optical counterpart in the USNO catalog, more than half of them could have $f_X > 0.1 f_R$, being consistent with a typical quasar. We note that nine sources satisfy the blank-source criteria ($f_X/f_V > 10$), as applied in Cagnoni et al. (2002). For these nine sources, we do not see any extra X-ray absorption, based on X-ray colors, consistent with Cagnoni et al. (2002). None of them are extended, but one of them could be variable. Among the sources (i.e., 3177 sources) found in CCDID = 0–3 in ACIS-I and CCDID = 6–7 in ACIS-S observations, we have identified 21 extended sources and 92 variable sources. They will be presented in a separate paper, along with the blank sources. The full ChaMP follow-up observations will provide statistical samples of a variety of intriguing objects with high-quality, unambiguous optical counterparts and an order of magnitude greater in quantity.

6. CONCLUSION

Analyzing $\sim$1000 near–on-axis X-ray–bright sources from an initial sample of 62 uniformly reduced *Chandra* observations, we conclude the following:

---

[2] See § 3.4 in Paper I and http://cxc.harvard.edu/cal/ASPECT/celmon.

[3] See, for example, the *ROSAT* WGA catalog by N. White, P. Giommi, & L. Angelini (1995) at http://heasarc.gsfc.nasa.gov/W3Browse/all/wgacat.html.

1. Our $\log N{-}\log S$ relation produced by the initial ChaMP sample is consistent with those seen by the CDFs and the previous missions. In particular, the H-band $\log N{-}\log S$ fills the gap between the CDF and *ASCA* data. The best-fit slopes for the S-band differential $\log N{-}\log S$ are $\beta_{\rm bright} = 2.2 \pm 0.2$ and $\beta_{\rm faint} = 1.4 \pm 0.3$ with $S_{\rm break} = (6 \pm 2) \times 10^{-15}$ ergs s^{-1} cm^{-2}, while $\beta = 2.1 \pm 0.1$ for the H-band differential $\log N{-}\log S$.

2. There is no statistically significant difference between the $\log N{-}\log S$ produced by fields containing clusters of galaxies and fields without clusters. Also, there is no statistically significant (within $\sim 1\ \sigma$) field-to-field variation in number densities of cosmic XRB sources in the flux range of $f_{\rm X} \sim 10^{-15}$ to 10^{-13} ergs s^{-1}.

3. The majority ($\sim$70%) of X-ray sources exhibit X-ray colors, typical of unabsorbed ($N_{\rm H}$ = a few $\times\ 10^{20}$ cm^{-2}) quasars (a photon index of $\sim$1.7). There also exist heavily absorbed or very soft/hard sources.

4. On average, the X-ray color becomes harder as the count rate decreases. It appears that this is mainly because of absorption rather than intrinsic spectral hardening because the hardening occurs in the soft color but does not exist in the hard color.

5. Cross-correlating with optical catalogs, we have divided X-ray sources into three groups: blue quasars, red quasars, and stars and normal galaxies. In the X-ray color-color plot, the blue quasars are heavily concentrated near the location of a typical unabsorbed power law. On the other hand, the stars/galaxies exhibit a wide spread and occupy a location with $kT < 1.5$ keV. Only a small number of red quasars are found, but from the full ChaMP sample we expect a considerable number of such sources that will allow us to test whether they are really obscured in either the optical or the X-ray band, or in both.

This work has been supported by Chandra X-Ray Center (CXC) archival research grant AR2-3009X. We acknowledge support through NASA contract NAS8-39073 (CXC). We thank the CXC DS and SDS teams for their support in pipeline processing and data analysis.

REFERENCES

Alexander, D. M., Vignali, C., Bauer, F. E., Brandt, W. N., Hornschemeier, A. E., & Garmire, G. P. 2002, AJ, 123, 1149

Baldi, A., Molendi, S., Comastri, A., Fiore, F., Matt, G., & Vignali, C. 2002, ApJ, 564, 190

Brandt, W. N., et al. 2001, AJ, 122, 2810

Cagnoni, I., Elvis, M., Kim, D.-W., Nicastro, F., & Celotti, A. 2002, ApJ, 579, 148

Cappi, M., et al. 2001, ApJ, 548, 624

Chandra X-Ray Center. 2000, *Chandra* Proposer's Observatory Guide, ver. 3.0

Comastri, A., Setti, G., Zamorani, G., & Hasinger, G. 1995, A&A, 296, 1

Condon, J. J., et al. 1998, AJ, 115, 1693

Cowie, L. L., Barger, A. J., Bautz, M. W., Brandt, W. N., & Garmire, G. P. 2003, ApJ, 584, L57

Cutri, R. M., et al. 2000, Explanatory Supplement to the 2MASS Second Incremental Data Release

Fabian, A. C., & Barcons, X. 1992, ARA&A, 30, 429

Gendreau, K. C., Barcons, X., & Fabian, A. C. 1998, MNRAS, 297, 41

Giacconi, R., et al. 2001, ApJ, 551, 624

Gilli, R., Rosati, G., & Salvati, M. 1999, A&A, 347, 424

Green, P. J., et al. 2004, ApJS, 150, 43

Gursky, H., & Schwartz, D. A. 1977, ARA&A, 15, 541

Hasinger, G., Burg, R., Giacconi, R., Schmidt, M., Trümper, J., & Zamorani, G. 1998, A&A, 329, 482

Hasinger, G., et al. 1993, A&A, 275, 1

———. 2001, A&A, 365, L45

Kenter, A. T., & Murray, S. S. 2003, ApJ, 584, 1016

Kim, D.-W., & Elvis, M. 1999, ApJ, 516, 9

Kim, D.-W., et al. 2004, ApJS, 150, 19 (Paper I)

Maccacaro, T., et al. 1988, ApJ, 326, 680

Marshall, F. E., Boldt, E. A., Holt, S. S., Miller, R. B., Mushotzky, R. F., Rose, L. A., Rothschild, R. E., & Serlemitsos, P. J. 1980, ApJ, 235, 4

Miyaji, T., Hasinger, G., & Schmidt, M. 2000, A&A, 353, 25

Monet, D., et al. 1998, USNO-A2.0 (Washington, DC: USNO)

Moretti, A., Campana, S., Lazzati, D., & Tagliaferri, G. 2003, ApJ, 588, 696

Murdoch, H. S., Crawford, D. F., & Jauncey, D. L. 1973, ApJ, 183, 1

Mushotzky, R. F., Cowie, L. L., Barger, A. J., & Arnaud, K. A. 2000, Nature, 404, 459

Ogasaka, Y., et al. 1998, Astron. Nachr., 319, 43

Rosati, P., et al. 2002, ApJ, 566, 667

Stark, A. A., et al. 1992, ApJS, 79, 77

Ueda, Y., et al. 1998, Nature, 391, 866

van Speybroeck, L. P., Jerius, D., Edgar, R. J., Gaetz, T. J., Zhao, P., & Reid, P. B. 1997, Proc. SPIE, 3113, 89

Vikhlinin, A., Forman, W., Jones, C., & Murray, S. S. 1995, ApJ, 451, 542

Webster, R. L., et al. 1995, Nature, 375, 469

Weisskopf, M. C., Tananbaum, H., van Speybroeck, L. P., & O'Dell, S. L. 2000, Proc. SPIE, 4012, 2

White, R. L., Becker, R. H., Helfand, D. J., & Gregg, M. D. 1997, ApJ, 475, 479

White, R. L., et al. 2003, AJ, 126, 706

Wilkes, B. J., et al. 2002, ApJ, 564, L65

Yang, L., et al. 2003, ApJ, 585, L85